PHOTONICS Research

Experimental demonstration of an electrically tunable broadband coherent perfect absorber based on a graphene–electrolyte–graphene sandwich structure

JIN ZHANG,[1] XINGZHAN WEI,[2] MALIN PREMARATNE,[3] AND WEIREN ZHU[1,*]

[1]Department of Electronic Engineering, Shanghai Jiao Tong University, Shanghai 200240, China
[2]Chongqing Institute of Green and Intelligent Technology, Chinese Academy of Sciences, Chongqing 400714, China
[3]Advanced Computing and Simulation Laboratory (AχL), Department of Electrical and Computer Systems Engineering, Monash University, Clayton, Victoria 3800, Australia
*Corresponding author: weiren.zhu@sjtu.edu.cn

Received 20 May 2019; revised 13 June 2019; accepted 13 June 2019; posted 14 June 2019 (Doc. ID 367969); published 18 July 2019

We propose and experimentally demonstrate the operation of an electrically tunable, broadband coherent perfect absorption (CPA) at microwave frequencies by harnessing the CPA features of a graphene–electrolyte–graphene sandwich structure (GSS). Using both a simplified lumped circuit model and full-wave numerical simulation, it is found that the microwave coherent absorptivity of the GSS can be tuned dynamically from nearly 50% to 100% by changing the Fermi level of the graphene. Strikingly, our simplified lumped circuit model agrees very well with the full-wave numerical model, offering valuable insight into the CPA operation of the device. The angle dependency of coherent absorption in the GSS is further investigated, making suggestions for achieving CPA at wide angles up to 80°. To show the validity and accuracy of our theory and numerical simulations, a GSS prototype is fabricated and measured in a C-band waveguide system. The reasonably good agreement between the experimental and the simulated results confirms that the tunable coherent absorption in GSS can be electrically controlled by changing the Fermi level of the graphene.

https://doi.org/10.1364/PRJ.7.000868

1. INTRODUCTION

A perfect absorber is a device that neither reflects nor transmits incident electromagnetic (EM) waves, which could be used for applications such as electromagnetic shielding [1,2] and ultrasensitive photo detection [3]. Since the pioneering work of Landy *et al.* [4] on a metamaterial perfect absorber (MPA) in 2008, different MPA structures have been designed and experimentally demonstrated for a wide range of frequencies, including microwave [5,6], terahertz [7,8], and optical frequencies [9,10]. However, the absorption performances in these MPAs are very much set at fabrication, limiting their applications to cases where flexible control of absorption is required. Recently, coherent perfect absorption (CPA), which arises from the interplay of interference and absorption, was demonstrated in a planar intrinsic silicon slab when illuminated on both sides by two counterpropagating beams with equal intensities and a preset phase difference between them [11,12]. The coherent absorption enhancement can also be extended to thin films, waveguides, and many other structures [13–16]. Compared to the perfect absorbers based on strong resonances, a CPA provides additional tunability of absorption through the interplay of interference. Therefore, it has great potential for applications in electromagnetic modulation, switching, and signal processing [17].

Thin films or slabs are the simplest structures for realizing CPA [13]. Particularly, two-dimensional (2D) materials [18–23] have ultralow profiles and possess excellent electrical properties for such realization. Significant efforts have been devoted to the theoretical exploration of CPA in graphene [24–28]. In the experimental aspect, Bae *et al.* [29] reported an efficient method for the synthesis and transfer of graphene, opening a new route to the low-cost production of high-quality monolayer graphene films suited for practical applications. Using single-layer graphene films, Li *et al.* [30] experimentally demonstrated that the static coherent absorption in graphene can be achieved over the X-band. Due to limited doping methods used in the microwave band, the graphene-based tunable microwave CPA has not yet been realized. Furthermore, the ability to dynamically control the conductivity of graphene via electrical doping enables one to experimentally observe the gate-tunable THz CPA in graphene-based cavities [31,32]. However, these graphene-based cavities operate as Salisbury screens, whose perfect absorptions are narrowband and limited by their thicknesses.

In this paper, we demonstrate both numerically and experimentally that electrically tunable and broadband CPA can be achieved in a graphene–electrolyte–graphene sandwich structure (GSS) whose thickness is less than 1/300 of the operating wavelength. We first show that the microwave coherent absorptivity can be tuned dynamically from around 50% to 100% by changing the Fermi level of graphene. To provide insight into the process, a simplified lumped circuit model is presented to explain the coherent absorption mechanism. Thereafter, we investigate the angular dependence of the coherent absorption in GSS. The tunability of GSS enables CPA for incident angles up to 80°. To strengthen our claims further, we fabricate a prototype of GSS and experimentally characterize it in a C-band waveguide system. The acceptable agreement between the experimental and simulated results shows that tunable coherent absorption in GSS can be controlled by applying different bias voltages.

2. EQUIVALENT LUMPED CIRCUIT MODEL

Figure 1(a) schematically shows the proposed GSS illuminated by two counter-propagating and coherently modulated input beams: I_+ and I_-; the corresponding output beams are given by O_+ and O_-. Here, the subscripts + and – refer to the forward and backward directions, respectively. The GSS consists of two graphene monolayers on 75 μm-thick polyvinylchloride (PVC) substrates ($\varepsilon_p = 3.6$) with an electrolyte layer between them. The electrolyte layer is made of a 50 μm thick diaphragm paper soaked with 20 μL ionic liquid. Due to the extremely low electron mobility in the electrolyte layer, the electrolyte itself could be reasonably considered as a dielectric with relative permittivity $\varepsilon_e = 2.4$. The vertical electrical bias between the top and the bottom graphene layers is generated by applying a voltage U across them. Thus, the positive and negative ions will concentrate toward the graphene electrodes and work as a supercapacitor. Because this setup enables the shifting of graphene's Fermi level when one varies the voltage across the supercapacitor setup, the structure

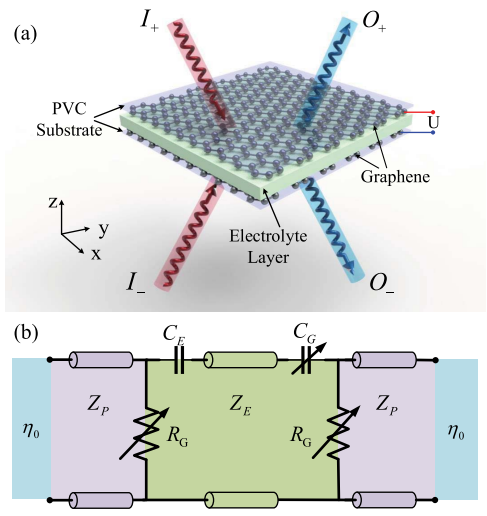

Fig. 1. (a) Schematic view of a GSS illustrated by two counter-propagating and coherently modulated input beams (I_+ and I_-), with O_+ and O_- being the output beams. (b) Equivalent circuit model of the GSS.

naturally lends itself to controllable features. The complex output beams $O_\pm$ of the GSS are related to the two input beams $I_\pm$ through a scattering matrix [14],

$$\begin{bmatrix} O_+ \\ O_- \end{bmatrix} = \begin{bmatrix} r_- & t_+ \\ t_- & r_+ \end{bmatrix} \begin{bmatrix} Ie^{i\varphi_+} \\ Ie^{i\varphi_-} \end{bmatrix}. \tag{1}$$

Without a loss of generality, for simplicity and clarity, we assume that the GSS is placed at the center of the two ports that generate forward and backward waves. Since the proposed GSS under investigation possesses reciprocity and spatial symmetry, the scattering matrix can be simplified with $t_- = t_+ = t$ and $r_- = r_+ = r$. The resulting scattering matrix has a symmetric eigenvector $[1, 1]^T$ and an antisymmetric eigenvector $[1, -1]^T$. For the GSS layer with a thickness much smaller compared to the working wavelength, the antisymmetric eigenvector corresponds to an eigenvalue of –1. This implies that the GSS is placed at a node of the standing wave, where electromagnetic losses become negligible. Therefore, the CPA in such a setup can only occur for the beams with symmetric incidence, corresponding to $I_+ = I_-$ (and phases match), where the coherent absorptivity can be expressed as [33]

$$A_c = 1 - \frac{|Q_+|^2 + |Q_-|^2}{|I_+|^2 + |I_-|^2} = 1 - |r + t|^2. \tag{2}$$

When the forward and backward incident beams are not phase matched and have a phase difference $\Delta\varphi = \varphi_+ - \varphi_-$ (i.e., $I_+ = I_- e^{-i\Delta\varphi}$), the total absorptivity becomes

$$A = 1 - \frac{|te^{-i\Delta\varphi} + r|^2 + |t + re^{-i\Delta\varphi}|^2}{2}. \tag{3}$$

To analytically calculate the scattering feature of the proposed GSS, an equivalent lumped circuit model is proposed in Fig. 1(b). In this model, the arrows represent the voltage-dependent circuit elements. Since graphene is sufficiently thin compared to the operating wavelength, it is modeled as a planar sheet with a complex surface conductivity (σ_g). The surface conductivity of graphene that contains intraband and interband contributions can be calculated with the random-phase approximation (RPA) formula [34], which is a function of temperature T, scattering rate τ, and Fermi level E_F. In the microwave frequency range ($\omega \gg \tau^{-1}$), graphene could be regarded as a resistive planar sheet with negligible dispersion. The sheet resistance (R_G) and the quantum capacitance (C_G) that depend on the Fermi level of graphene can be calculated as [35,36]

$$R_G = \frac{1}{\sigma_g} = \frac{\pi\hbar^2(\omega - j\tau^{-1})}{-j2e^2k_BT} \log^{-1}\left[2\cosh\left(\frac{E_F}{2k_BT}\right)\right], \tag{4}$$

$$C_G = 2e^2D = \sqrt{n/\pi}(4e^2/\hbar v_F), \tag{5}$$

where e is the electron charge, and k_B and $\hbar$ are the Boltzmann constant and the reduced Planck constant (Dirac constant), respectively. In our case, we assume the room temperature is $T = 300$ K and the scattering rate is $\tau = 0.5$ ps; D is the density of states, $v_F \approx c/300$ is the Fermi velocity of the Dirac electron [35], $n \approx 8 \times 10^{11}$ cm^{-2} is the charge concentration [37], and C_E represents the electrostatic capacitance of the electrolyte layer, and its value is about 30 μF/cm^2 [38]. In terms of transverse electromagnetic transmission line theory [39], the PVC substrate and the electrolyte layer can be modeled as a dielectric

with the propagation constant $\beta_{p,e}$ and the characteristic impedance $Z_{p,e}$. The thicknesses of the PVC substrate and the electrolyte layer are 75 μm and 50 μm, respectively. η_0 is the characteristic impedance of free space. The general analytical expressions of the propagation constants and the characteristic impedance in the PVC and electrolyte layers for TE and TM polarizations could be written as [40]

$$\beta_{p,e} = \frac{\omega}{c}\cos\theta\sqrt{\varepsilon_{p,e} - \sin^2\theta}, \tag{6}$$

$$Z_0^{\mathrm{TE}} = \frac{\eta_0}{\cos\theta}, \tag{7a}$$

$$Z_0^{\mathrm{TM}} = \eta_0\cos\theta, \tag{7b}$$

$$Z_{p,e}^{\mathrm{TE}} = \frac{\eta_0}{\sqrt{\varepsilon_{p,e} - \sin^2\theta}}, \tag{8a}$$

$$Z_{p,e}^{\mathrm{TM}} = \frac{\eta_0\sqrt{\varepsilon_{p,e} - \sin^2\theta}}{\varepsilon_{p,e}}, \tag{8b}$$

where c is the speed of light in vacuum, ω is the angular frequency, θ is the angle of the incident beams, and $\eta_0 = \sqrt{\mu_0/\varepsilon_0}$ is the wave impedance of the free space. Furthermore, the transfer matrix method can be used to describe the reflection coefficient r and transmission coefficient t from the GSS in a two-port system [41],

$$t = \frac{A + B/Z_0 - CZ_0 - D}{A + B/Z_0 + CZ_0 + D}, \tag{9a}$$

$$r = \frac{2(AD - BC)}{A + B/Z_0 + CZ_0 + D}, \tag{9b}$$

and

$$\begin{bmatrix} A & B \\ C & D \end{bmatrix} = M_p M_R \begin{bmatrix} 1 & C_E \\ 0 & 1 \end{bmatrix} M_e \begin{bmatrix} 1 & C_G \\ 0 & 1 \end{bmatrix} M_R M_p. \tag{10}$$

Here,

$$M_{p,e} = \begin{bmatrix} \cos(\beta_{p,e}h_{p,e}) & jZ_{p,e}\sin(\beta_{p,e}h_{p,e}) \\ j\sin(\beta_{p,e}h_{p,e})/Z_{p,e} & \cos(\beta_{p,e}h_{p,e}) \end{bmatrix}, \tag{11a}$$

$$M_R = \begin{bmatrix} 1 & 0 \\ 1/R_G & 1 \end{bmatrix}. \tag{11b}$$

3. NUMERICAL SIMULATION RESULTS

We have used both a simplified lumped circuit model and full-wave numerical simulations (CST Microwave Studio, version 2018, commercial software) to study the performance of the GSS. Figure 2 shows the tunable coherent absorptivity of the GSS under different values of Fermi levels. It is clearly seen that the analytical calculations and the numerical simulations are in very good agreement with each other, confirming the validity and accuracy of our lumped circuit model. Figure 2 also shows that the coherent absorptivity increases when the Fermi level is increased. In particular, the change of the Fermi level from 0 to 0.2 eV maps the increase of the coherent absorptivity from 52% to 100%. The coherent absorptivity reaches 100% when the Fermi level of graphene reaches 0.2 eV, in which case the scattering from both sides of the GSS is completely suppressed. When further increasing the Fermi level from 0.2 eV to 1 eV, the coherent absorptivity starts to decrease from 100% to 60%. Moreover, these coherent absorptivity curves are nearly frequency independent within the frequency range of interest. The intrinsic broadband feature of this structure comes from the nearly nondispersive surface conductivity of graphene at microwave frequencies, which is significantly different for graphene at THz or optical frequencies.

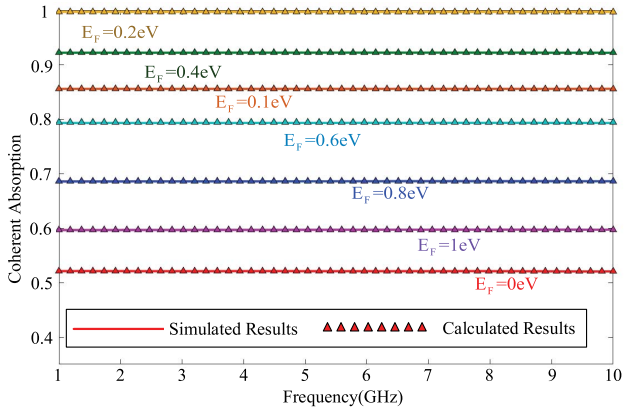

Fig. 2. Coherent absorption of GSS for plane wave versus frequency under different Fermi levels. The solid line represents the 3D full wave simulation results and dotted line means the equivalent circuit calculated results.

To further investigate the coherent absorption process with a GSS, in Fig. 3 we plot the calculated and simulated false-color

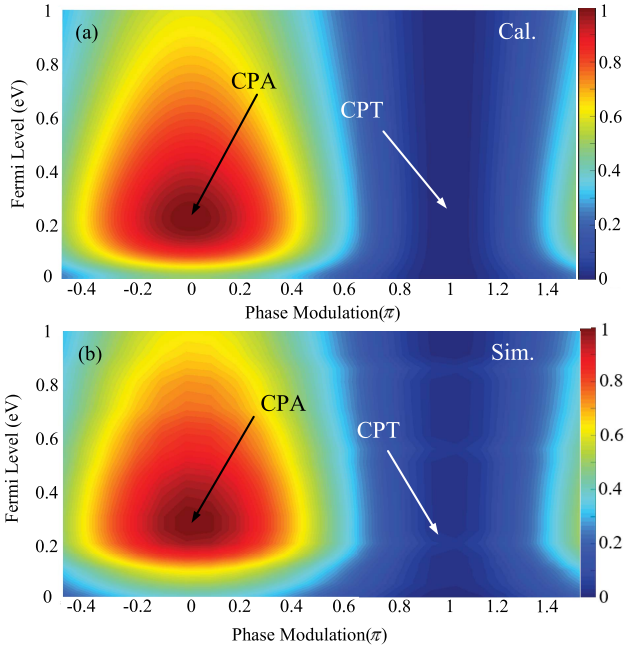

Fig. 3. Two-dimensional false-color plot of the calculated coherent absorption as a function of Fermi level and phase modulation. (a) Equivalent circuit calculated results and (b) simulated results.

map of the coherent absorptivity at 4 GHz, which shows the strong dependence on the graphene's Fermi level and the phase modulation ($\Delta\varphi$) of the two input beams. It is clearly seen from this figure that proper phase matching ($\Delta\varphi = 0$) in conjunction with a correctly set Fermi level ($E_F = 0.22$ eV) leads to nearly complete CPA. Note that, the coherent absorptivity decreases to nearly zero on the conditions of $\Delta\varphi = \pi$ and $E_F = 0.22$ eV, meaning that the coherent perfect transparency (CPT) can also be realized. Furthermore, a substantial continuous modulation of the coherent absorption with the phase difference $\Delta\varphi$ is also found in both calculated and simulated results. At $E_F = 0.22$ eV, the corresponding coherent absorptivity can be modulated from 0.01% to 99.97% by changing the phase difference between the two input beams. This implies that coherent beams propagating through the GSS can be modulated from an almost entirely absorbed state to an almost entirely transparent state.

Angular selectivity, or spatial dispersion, is a fundamental feature for the realization of wave selection. Because of the tunability of graphene, the GSS-based CPA can also be realized for an oblique incidence. The coherent absorption for both TE and TM incidences is calculated and plotted in Figs. 4(a) and 4(b), respectively, showing that coherent absorption of the GSS is sensitive to both the polarization and incident angle. In particular, when the Fermi level is set to 0.2 eV, the dashed lines in Figs. 4(a) and 4(b) show that the coherent absorption decreases from nearly 100% to less than 50% as the incident angle of TE/TM wave increases from 0° to 90°. Despite this sensitivity, setting the Fermi level of graphene is still an efficient method to realize CPA with a large incident angle up to 80°. Figure 4(c) clearly shows that the CPA Fermi level splits into two branches for orthogonal TE and TM polarizations. For TE polarization, the CPA Fermi level has a decrease with respect to the normal incident CPA point; for the TM polarization, the CPA Fermi level increases with respect to the normal incident CPA point. The two bands touch each other and cover a large incident angle range from 0° to nearly 80°. This implies that the CPA with

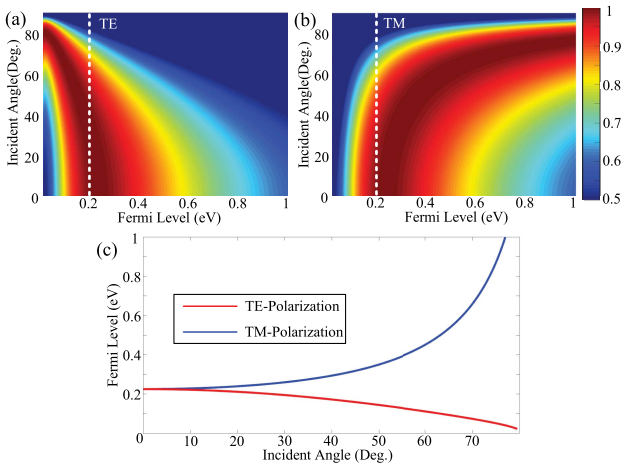

Fig. 4. (a) and (b) Calculated coherent absorption under TE/TM incident illumination, where the dashed lines denote the condition of $E_F = 0.22$ eV. (c) CPA Fermi-level dispersion at an oblique incidence for TE polarization (red solid curve) and TM polarization (blue solid curve).

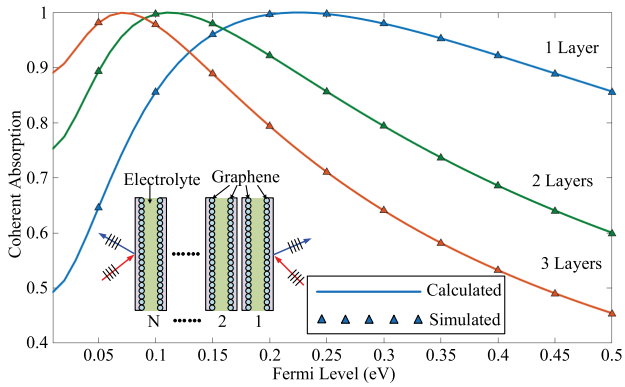

Fig. 5. Coherent absorption of N-layers stacked GSS versus Fermi energy. Insert graph is the schematic of stacked GSS illuminated by two counter-propagating input beams. Solid curves represent the equivalent circuit calculated results and triangles refer to the full-wave simulation results.

large incident angle for either TE or TM polarization could be realized by increasing or decreasing the Fermi level.

Theoretically, the Fermi level of graphene in GSS can be manipulated efficiently by applying a bias voltage. However, in practice, it is difficult to achieve a high Fermi level in GSS. Previous work has demonstrated experimentally that when the bias voltage increases from 0 V to 4 V, the sheet resistance of GSS decreases from 3000 Ω to 500 Ω [42]. According to Eq. (3), it can be derived that the practical Fermi level of graphene in GSS could be tuned from 0 eV to 0.18 eV by applying the bias voltage from 0 V to 4 V, which is slightly lower than the required CPA Fermi level (0.22 eV). To overcome this issue, we propose an alternative approach by stacking multiple layers of GSS. Figure 5 shows a schematic view of the N layers of the stacked GSS and the calculated coherent absorptivities. Based on the equivalent circuit theory, the stacked GSS layers are equivalent to the parallel connection of the GSS layers. The resulting transfer matrix can be written as

$$\begin{bmatrix} A_N & B_N \\ C_N & D_N \end{bmatrix} = \begin{bmatrix} A & B \\ C & D \end{bmatrix} \cdots \begin{bmatrix} A & B \\ C & D \end{bmatrix} = \begin{bmatrix} A & B \\ C & D \end{bmatrix}^N, \tag{12}$$

where N represents the number of the stacked layers. When stacking multiple GSS layers, shown in the insert of Fig. 5, the resistive contribution of the whole stacked structure can be approximately taken as $R_G/2N$. The analytical and simulated coherent absorptivity curves for the cases of one, two, and three layers of GSS are shown in Fig. 5. It is found that the CPA Fermi level decreases from 0.22 eV to 0.07 eV when the number of stacked layers increases from one to three. These results confirm that stacking layers of GSS is an efficient way to realize coherent perfect absorption in GSS under a low-set Fermi level.

4. EXPERIMENTAL RESULTS

To fabricate the GSS, we have synthesized monolayer graphene on copper foil using the large-diameter chemical vapor deposition (CVD) method. The 532-nm laser-excited Raman spectroscopy is used to evaluate the quality of graphene on a SiO_2/Si substrate. Figure 6(b) shows a typical Raman spectrum, where

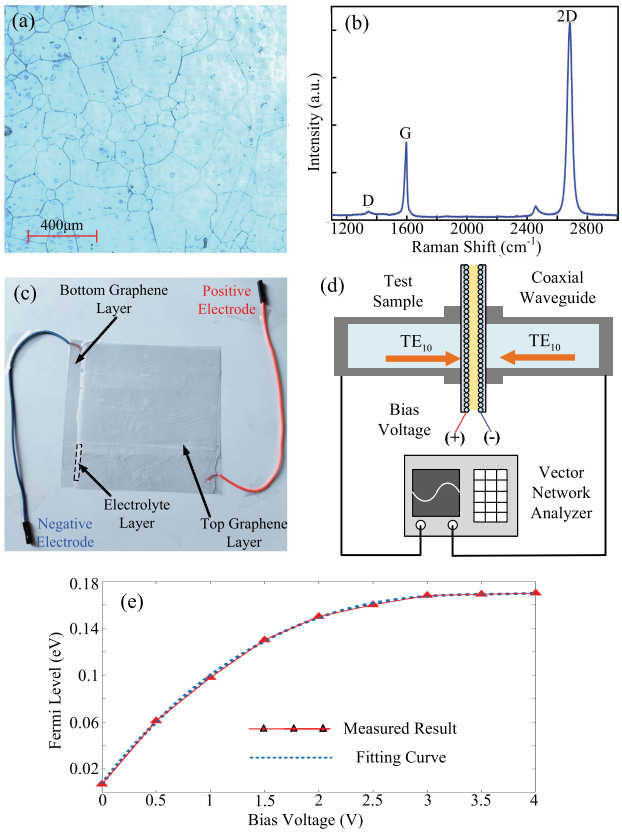

Fig. 6. (a) Optical image of graphene on a PVC substrate. (b) Raman spectrum of monolayer graphene. (c) Fabricated GSS device. (d) Configuration of the waveguide measurement setup. (e) Relation between the Fermi level of graphene and bias voltage.

the G-peak (1590 cm^{-1}) and the 2D peak (2687 cm^{-1}) are shown. The intensity ratio I_{2D}/I_G is about 2.4 and the full width at half maximum of the 2D peak is about 31 cm^{-1}. These results confirm that our fabricated graphene is monolayer with a thickness around 0.34 nm. Furthermore, the disorder-induced D peak (1345 cm^{-1}) is very weak, indicating the high quality of our fabricated graphene. The prepared monolayer graphene is then transferred onto flexible PVC substrates using a hot lamination technique. Thereafter, nitric acid with a 65% concentration is used to etch the laminated copper foil. Figure 6(a) shows an optical image of graphene on a PVC substrate where the graphene lattices are clearly visible. The completed monolayer graphene/PVC film is diluted by deionized (DI) water to remove the residual nitric acid and other impurities. Next, a piece of diaphragm paper (porous membrane) with a thickness of 50 μm is placed between the two prepared graphene/PVC films as a separating layer. The whole setup is then soaked in 20 μL ionic liquid ([DEME][TFSI]) to finally make the GSS. The final structure of the fabricated GSS is shown in Fig. 6(c). Applying bias voltages will efficiently polarize the ionic liquid in the membrane. Since the electrolyte layer is very thin, the GSS works as a supercapacitor and yields a very large electric field, which can electrostatically vary the Fermi level of the two graphene layers, enabling one to electrically vary the absorption performance of graphene [38]. The 75 μm-thick PVC substrate (relative permittivity of 3.6) and the 50 μm diaphragm paper (relative permittivity of 2.5) are almost fully transparent in the microwave band. In particular, the whole GSS is only about 200 μm thick, which is equal to 1/375 of the free space wavelength at 4 GHz.

The relation between the measured Fermi level of graphene and the bias voltage is shown in Fig. 6(e). The Fermi level of graphene increases monotonously from nearly 0 to 0.17 eV while the voltage increases from 0 to 4 V. Furthermore, to determine this relation quantitatively, an empirical formula and the corresponding curve based on the fitting polynomial method are provided in Fig. 6(e). With this fitting curve, the approximate Fermi level of graphene under a different bias voltage can be calculated easily and rapidly.

Although large-scale monolayer graphene currently can be synthesized by the CVD method, the cost to synthesize large samples for free space measurement in the microwave band is still prohibitively high. Thus, to validate the results of our design in a cost-effective way, a waveguide system is set up for the measurement of the GSS reflection and transmission, as shown in Fig. 6(d). We employ a microwave network analyzer (Agilent N5230C) and connect two identical coax-to-waveguide adapters (WR-229) with ports 1 and 2 of the analyzer. The electromagnetic waves inside the waveguide are equivalent to obliquely incident plane waves with an incident angle given by $\theta_0 = \arccos(\lambda_0/\lambda_g)$ [43], where λ_g is the guided wavelength. To ensure that the waveguide excites its dominant TE_{10} mode, measurements are carried out below the TE_{20} cutoff frequency of 5 GHz. After calibrating the bare setup using the through-reflect-line method, the GSS sample was placed in the middle of the two waveguides for measurements and the TE_{10} polarized waves are launched from both sides with same phases. Different bias voltages were applied to the graphene layers and the corresponding parameters were recorded. The coherent absorptivities were then calculated according to Eq. (2). The measured coherent absorptivities were plotted as circles in Fig. 7(a), where the solid lines are the corresponding analytical results. It is

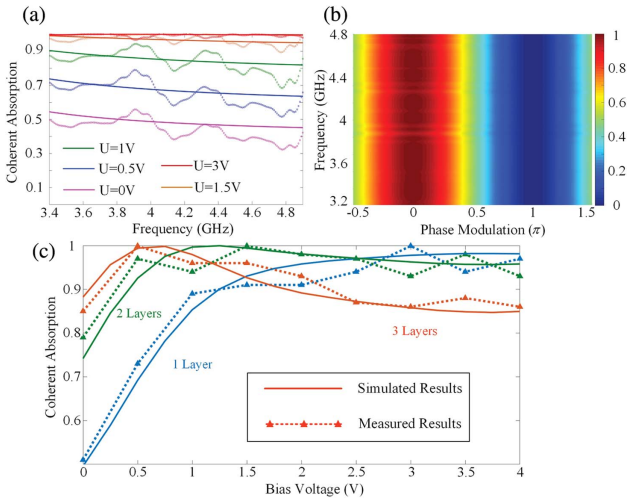

Fig. 7. (a) Measured (circles) and calculated (solid lines) coherent absorptivities of GSS in the waveguide system under different bias voltages. (b) A 2D false-color plot of the coherent absorptivity as a function of frequency and phase modulation ($U = 3$ V). (c) Coherent absorption of single- or multilayered GSS versus bias voltage ($f = 4.27$ GHz).

seen that the measured coherent absorptivity raises from less than 50% to nearly 100% with the bias voltage increasing from 1 V to 3 V. Note that when the bias voltage is higher than 1.5 V, the coherent absorptivity is higher than 90% in the entire frequency range from 3.4 GHz to 4.9 GHz. In particular, the nearly perfect coherent absorptivity (99.79%) appears at a bias voltage of 3 V. The deviations are mainly due to the inhomogeneity of the synthesized graphene layers. It is worth noting that the measured coherent absorptivity increases monotonously when the voltage increases from 0 to 3 V. This is in accordance with the calculations in Fig. 5, for the case when the Fermi level increases from 0 to 0.2 eV. Further increasing the bias voltage in theory could decrease the coherent absorptivity, but this action is difficult to reasonably achieve.

In Fig. 7(b), we show the modulation of the measured coherent absorption in the GSS by controlling the phase difference between the two input ports. It is seen that, when the bias voltage is 3 V, the coherent absorptivity varies continuously from nearly 100% to less than 5% as the phase difference $\Delta\varphi$ changes from -0.5π to 1.5π, giving a modulation contrast of 30 dB. It also shows that the CPA of the GSS could be realized in a broad band from 3.2 GHz to 4.8 GHz, indicating clearly that the GSS is nearly insensitive to the working frequency. Furthermore, the experimental coherent absorptions for multiple GSS layers under different bias voltages are shown in Fig. 7(d). Compared to a single GSS layer, lower bias voltages are required to achieve CPA in a multilayer GSS. The reasonably good agreement between the measured and simulated results also verifies our analysis shown in Fig. 5.

5. CONCLUSION

In conclusion, we have numerically investigated and experimentally demonstrated electrically tunable, broadband CPA in a graphene–electrolyte–graphene sandwiched structure (GSS). By electrically gating the Fermi level of graphene in a relatively low range from 0 to 0.22 eV, the coherent absorptivity of the GSS could be dynamically tuned from 50% to 100%. Full-wave simulations and experimental measurements show good agreement between each other. We gained further insight into the design by developing a simplified lumped circuit model, showing remarkable agreement with both experimental and simulation results. Moreover, we show that frequency-independence coherent absorption could be realized for either TE or TM polarization at incident angles up to 80°. Our work enables ultra-broadband, wide-angle applications in microwave absorbers and may bridge two important technological fields: 2D materials and signal processing.

Funding. National Natural Science Foundation of China (NSFC) (11574308, 61701303); Natural Science Foundation of Shanghai (17PJ1404100, 17ZR1414300).

REFERENCES

1. D. Shrekenhamer, J. Montoya, S. Krishna, and W. J. Padilla, "Four-color metamaterial absorber THz spatial light modulator," Adv. Opt. Mater. **1**, 905–909 (2013).
2. S. Savo, D. Shrekenhamer, and W. J. Padilla, "Liquid crystal metamaterial absorber spatial light modulator for THz applications," Adv. Opt. Mater. **2**, 275–279 (2014).
3. F. Zhao, C. Zhang, H. Chang, and X. Hu, "Design of plasmonic perfect absorbers for quantum-well infrared photodetection," Plasmonics **9**, 1397–1400 (2014).
4. N. I. Landy, S. Sajuyigbe, J. J. Mock, D. R. Smith, and W. J. Padilla, "Perfect metamaterial absorber," Phys. Rev. Lett. **100**, 207402 (2008).
5. S. Zhong and S. He, "Ultrathin and lightweight microwave absorbers made of mu-near-zero metamaterials," Sci. Rep. **3**, 2083 (2013).
6. B. Wang, T. Koschny, and C. M. Soukoulis, "Wide-angle and polarization-independent chiral metamaterial absorber," Phys. Rev. B **80**, 033108 (2009).
7. R. Alaee, M. Farhat, C. Rockstuhl, and F. Lederer, "A perfect absorber made of a graphene micro-ribbon metamaterial," Opt. Express **20**, 28017–28024 (2012).
8. X. Xiong, S.-C. Jiang, Y.-H. Hu, R.-W. Peng, and M. Wang, "Structured metal film as a perfect absorber," Adv. Mater. **25**, 3994–4000 (2013).
9. M. K. Hedayati, M. Javaherirahim, B. Mozooni, R. Abdelaziz, A. Tavassolizadeh, V. S. K. Chakravadhanula, V. Zaporojtchenko, T. Strunkus, F. Faupel, and M. Elbahri, "Design of a perfect black absorber at visible frequencies using plasmonic metamaterials," Adv. Mater. **23**, 5410–5414 (2011).
10. B. Zhang, Y. Zhao, Q. Hao, B. Kiraly, I.-C. Khoo, S. Chen, and T. J. Huang, "Polarization-independent dual-band infrared perfect absorber based on a metal-dielectric-metal elliptical nanodisk array," Opt. Express **19**, 15221–15228 (2011).
11. Y. D. Chong, L. Ge, H. Cao, and A. D. Stone, "Coherent perfect absorbers: time-reversed lasers," Phys. Rev. Lett. **105**, 053901 (2010).
12. W. Wan, Y. Chong, L. Ge, H. Noh, A. D. Stone, and H. Cao, "Time-reversed lasing and interferometric control of absorption," Science **331**, 889–892 (2011).
13. S. Li, J. Luo, S. Anwar, S. Li, W. Lu, Z. H. Hang, Y. Lai, B. Hou, M. Shen, and C. Wang, "Broadband perfect absorption of ultrathin conductive films with coherent illumination: superabsorption of microwave radiation," Phys. Rev. B **91**, 220301 (2015).
14. W. Zhu, F. Xiao, M. Kang, and M. Premaratne, "Coherent perfect absorption in an all-dielectric metasurface," Appl. Phys. Lett. **108**, 121901 (2016).
15. R. Bruck and O. L. Muskens, "Plasmonic nanoantennas as integrated coherent perfect absorbers on SOI waveguides for modulators and all-optical switches," Opt. Express **21**, 27652–27661 (2013).
16. M. Kang, Y. D. Chong, H.-T. Wang, W. Zhu, and M. Premaratne, "Critical route for coherent perfect absorption in a Fano resonance plasmonic system," Appl. Phys. Lett. **105**, 131103 (2014).
17. X. Fang, M. Lun Tseng, J.-Y. Ou, K. F. MacDonald, D. P. Tsai, and N. I. Zheludev, "Ultrafast all-optical switching via coherent modulation of metamaterial absorption," Appl. Phys. Lett. **104**, 141102 (2014).
18. Y. Wang, W. Huang, C. Wang, J. Guo, F. Zhang, Y. Song, Y. Ge, L. Wu, J. Liu, and J. Li, "An all-optical, actively Q-switched fiber laser by an antimonene-based optical modulator," Laser Photon. Rev. **13**, 1800313 (2019).
19. Y. Wang, F. Zhang, X. Tang, X. Chen, Y. Chen, W. Huang, Z. Liang, L. Wu, Y. Ge, and Y. Song, "All-optical phosphorene phase modulator with enhanced stability under ambient conditions," Laser Photon. Rev. **12**, 1800016 (2018).
20. X. Jiang, S. Liu, W. Liang, S. Luo, Z. He, Y. Ge, H. Wang, R. Cao, F. Zhang, and Q. Wen, "Broadband nonlinear photonics in few-layer MXene $Ti_3C_2T_x$ (T = F, O, or OH)," Laser Photon. Rev. **12**, 1700229 (2018).
21. A. K. Geim and K. S. Novoselov, "The rise of graphene," Nat. Mater. **6**, 183–191 (2007).
22. A. H. Castro Neto, F. Guinea, N. M. R. Peres, K. S. Novoselov, and A. K. Geim, "The electronic properties of graphene," Rev. Mod. Phys. **81**, 109–162 (2009).
23. Y. Fan, N.-H. Shen, F. Zhang, Q. Zhao, H. Wu, Q. Fu, Z. Wei, H. Li, and C. M. Soukoulis, "Graphene plasmonics: a platform for 2D optics," Adv. Opt. Mater. **7**, 1800537 (2019).
24. G. Pirruccio, L. Martín Moreno, G. Lozano, and J. Gómez Rivas, "Coherent and broadband enhanced optical absorption in graphene," ACS Nano **7**, 4810–4817 (2013).
25. S. M. Rao, J. J. F. Heitz, T. Roger, N. Westerberg, and D. Faccio, "Coherent control of light interaction with graphene," Opt. Lett. **39**, 5345–5347 (2014).

26. J. R. Piper and S. Fan, "Total absorption in a graphene monolayer in the optical regime by critical coupling with a photonic crystal guided resonance," ACS Photon. **1**, 347–353 (2014).
27. Y. Fan, F. Zhang, Q. Zhao, Z. Wei, and H. Li, "Tunable terahertz coherent perfect absorption in a monolayer graphene," Opt. Lett. **39**, 6269–6272 (2014).
28. V. Thareja, J.-H. Kang, H. Yuan, K. M. Milaninia, H. Y. Hwang, Y. Cui, P. G. Kik, and M. L. Brongersma, "Electrically tunable coherent optical absorption in graphene with ion gel," Nano Lett. **15**, 1570–1576 (2015).
29. S. Bae, H. Kim, Y. Lee, X. Xu, J.-S. Park, Y. Zheng, J. Balakrishnan, T. Lei, H. R. Kim, and Y. I. Song, "Roll-to-roll production of 30-inch graphene films for transparent electrodes," Nat. Nanotechnol. **5**, 574–578 (2010).
30. S. Li, Q. Duan, S. Li, Q. Yin, W. Lu, L. Li, B. Gu, B. Hou, and W. Wen, "Perfect electromagnetic absorption at one-atom-thick scale," Appl. Phys. Lett. **107**, 181112 (2015).
31. F. Liu, Y. D. Chong, S. Adam, and M. Polini, "Gate-tunable coherent perfect absorption of terahertz radiation in graphene," 2D Mater. **1**, 031001 (2014).
32. N. Kakenov, O. Balci, T. Takan, V. A. Ozkan, H. Altan, and C. Kocabas, "Observation of gate-tunable coherent perfect absorption of terahertz radiation in graphene," ACS Photon. **3**, 1531–1535 (2016).
33. W. Zhu, F. Xiao, M. Kang, D. Sikdar, X. Liang, J. Geng, M. Premaratne, and R. Jin, "MoS_2 broadband coherent perfect absorber for terahertz waves," IEEE Photon. J. **8**, 5502207 (2016).
34. G. W. Hanson, "Dyadic Green's functions and guided surface waves for a surface conductivity model of graphene," J. Appl. Phys. **103**, 064302 (2008).
35. J. Xia, F. Chen, J. Li, and N. Tao, "Measurement of the quantum capacitance of graphene," Nat. Nanotechnol. **4**, 505–509 (2009).
36. L. A. Ponomarenko, R. Yang, R. V. Gorbachev, P. Blake, A. S. Mayorov, K. S. Novoselov, M. I. Katsnelson, and A. K. Geim, "Density of states and zero landau level probed through capacitance of graphene," Phys. Rev. Lett. **105**, 136801 (2010).
37. S. Adam, E. H. Hwang, V. M. Galitski, and S. Das Sarma, "A self-consistent theory for graphene transport," Proc. Natl. Acad. Sci. USA **104**, 18392–18397 (2007).
38. E. O. Polat and C. Kocabas, "Broadband optical modulators based on graphene supercapacitors," Nano Lett. **13**, 5851–5857 (2013).
39. N. Marcuvitz, *Waveguide Handbook* (IET, 1951).
40. Y. R. Padooru, A. B. Yakovlev, C. S. R. Kaipa, F. Medina, and F. Mesa, "Circuit modeling of multiband high-impedance surface absorbers in the microwave regime," Phys. Rev. B **84**, 035108 (2011).
41. T. Zhan, X. Shi, Y. Dai, X. Liu, and J. Zi, "Transfer matrix method for optics in graphene layers," J. Phys. Condens. Matter **25**, 215301 (2013).
42. A. Zhang, Z. Liu, W. Lu, and H. Chen, "Dynamically tunable attenuator on a graphene-based microstrip line," IEEE Trans. Microw. Theory Tech. **67**, 746–753 (2019).
43. D. Kundu, R. K. Gayen, A. Mohan, and A. Chakrabarty, "Moment method analysis of periodic array of thin conducting strips using waveguide simulator," J. Electromagn. Waves Appl. **32**, 363–370 (2018).